JOURNAL OF MATERIALS SCIENCE 31 (1996) 2097–2108

Behaviour of Hastelloy C22 steel in sulphate solutions at pH 3 and low temperatures

G. BELLANGER*
Commissariat à l'Energie Atomique, Centre d'Etudes de Valduc, F21120 Is sur Tille, France
J. J. RAMEAU
CREMGP, ENSEEG/INPG, Domaine Universitaire, B.P. 75, F38402 Saint Martin d'Hères, France

The behaviour of Hastelloy C22 steel (N06022 UNS) in solutions at pH 3 and different temperatures, for radioactive water reprocessing plants was studied. The corrosion potential was found to increase with temperature. In the neighbourhood of the active–passive potentials, Hastelloy steel was corroded by means of a transient form. In addition, the potentials of the active and transpassive peaks shifted towards more negative values with increasing temperature. The transpassive peak increased with temperature and its potential shifted towards smaller values. The temperature increase led to a reduction of the passive region and a higher current in the passivity. As shown by current instabilities during the backward scan and a higher current than those in the forward transpassivity scan, all of the oxide layer could not be destroyed at the breakdown transpassive potentials. From electrochemical impedance spectroscopy (EIS), apparently the thickness of the passive oxide decreased with temperature in the prepassive region. In passivity, the EIS showed an enhancement of corrosion for higher potentials or temperatures. At the passivity–transpassivity limit potentials, an inductive loop may be the result of adsorption. It was found that the diameter of the capacitive semi-circle and the inductive loop decreased when the temperature increased, indicating an enhancement of corrosion and a decrease in adsorption. The number of active sites and oxidation rate were determined at different potentials.

1. Introduction

A study was carried out to ascertain the corrosion behaviour of Hastelloy steel in a radioactive aqueous medium, in this case, tritiated water. The tritium in tritiated water decays with the emission of a β^- particle and a γ_e antineutrino. The energy released in this decay is 5.7 keV per tritium atom and is high enough to decompose locally the molecules of water along the path of the β^- particle with the formation of hydrogen peroxide. Depending on the storage conditions, in an open or closed container, the hydrogen peroxide concentration varies over a wide range. The effects of H_2O_2 were not determined here; the behaviour of H_2O_2 and the energy released were reported in previous publications [1, 2]. Quantitative analysis of tritium distributions and stress corrosion cracking in stainless steels was reported by Chêne and co-workers [3, 4]. If tritiated water is not stored for long periods in closed containers, the concentration of radiolytic products is low, which leads the corrosion, free and redox potentials towards a value situated near the active region of Hastelloy steel. At high pressure, these potentials should be in the passive–transpassive region due to an over oxygenation by radiolysis. Depending on reprocessing conditions, the potential may also be imposed in this same region. An acidic medium was selected because relatively concentrated acid solutions are produced in tritiated water reprocessing installations during the course of the catalytic gaseous tritium oxidation cycles at 450 °C with air and finely divided palladium. This can be explained by the effect of β^- particles on the nitrogen in the air used for oxidation in tritiated water; the reactions are from Bruggeman *et al.* [5], Burns and Moore [6], Linacre and Marsh [7], Wright *et al.* [8]

$$N_2 + \beta^- \rightarrow 2\,N^{\cdot} \quad (1)$$

$$N^{\cdot} + 3HO_2^- \rightarrow HNO_3 + H_2O + 2O^{\cdot} \quad (2)$$

The HO_2^- radical is an intermediate species produced in water radiolysis. Thus, the final products from the catalytic cycles give an appreciable nitric acid concentration. If the tritiated water radioactivity is very high, e.g. 70 TBq cm^{-3}, radiolytic gas bubbles are formed quickly and the temperature of tritiated water is much higher than the ambient due to the energy of β^-

* Author to whom all correspondence should be addressed.

0022–2461

particles and free radicals leading to a blue luminescence. Depending on reprocessing conditions, the tritiated water can also be heated.

It is essential in such highly concentrated tritiated water reprocessing facilities that there are no leaks from the processing circuit to the environment. Organic polymers, seal or pump oils are decomposed by reactions induced by the energy released from β^- particles and cannot be used. To avoid corrosion, using very highly radioactive aqueous solutions, the new equipment must be completely constructed of stainless steel. Because all the equipment in the facility is metallic, the selection of steel alloys depends not only on their corrosion resistance but also on their hardness; low- and high-hardness alloys are required. A low-hardness component (e.g., N06022 UNS steel) is assembled with a high-hardness component to ensure that the joints are perfectly tight. The present study was designed to examine the characteristic values of the Hastelloy steel using electrochemical impedance spectroscopy. For better understanding and comparisons, the electrochemical investigations were also supplemented by anodic polarization and cyclic voltammetry measurements at low and high scan rates. Because of the redox potential values in tritiated water, the selected potentials are situated at the corrosion potential, in the prepassivity, passivity and passivity–transpassivity limit.

2. Experimental procedure

The voltammetric equipment consisted of a Tacussel bipotentiostat and signal generator (PRT-20 and GSTP 3) connected to a Tektronix 2230 digital oscilloscope and a Hewlett–Packard HP 7440 AXY plotter. The impedance diagrams, and anodic polarization curves were drawn by a ZCP 130T Tacussel computer controlled by a 486-25U Vectra Hewlett–Packard personal computer, using the same plotter. The curves were plotted using a Hastelloy C22 steel electrode with a surface of 0.2 cm^2 whose rotation rate (r.p.m.) was determined in each test. The Hastelloy C22 disc electrode, manufactured by the Tacussel firm, consisted of a Hastelloy C22 rod well embedded in a Teflon cylindrical tube to avoid electrolytic infiltration, which would modify the curve shape. The electrode was pretreated always following the same procedure to obtain good reproducibility of the data. Prior to each use, the Hastelloy C22 electrode (disc) was mechanically polished using 1000 mesh grade silicon carbide sheets, then with diamond paste down to 1 μm and washing with deionized water. In this way, the electrode acquired a reproducible silvery bright surface. The roughness factor, r, for polished Hastelloy C22 is estimated to be in the range 1–1.6 [9–14]. For our experiments, we assume that the factor is 1.1. The temperature of the electrochemical cell was maintained at $\pm 0.2\,^{\circ}C$ by flowing water from a thermostatted reservoir. The electrolyte was deaerated by nitrogen bubbling before measurement runs to remove oxygen. pH 3 was obtained by the addition of H_2SO_4, but not by addition of a buffer, which could adsorb on the Hastelloy surface. Sodium sulphate was used as a support electrolyte at a concentration of 0.1 or 1 $mol\,dm^{-3}$ to compensate the ohmic-drop effect. The electrolyte was prepared from analytical grade reagents (Merck). In order to perform impedance measurements, several precautions are necessary. Short connection leads were used to minimize inductance effects. Additionally, to avoid capacitive interferences at the reference electrode, a platinum wire was connected to the reference electrode through a 0.1 μF capacitance. The Hastelloy C22 electrode potentials were related to a saturated calomel electrode (SCE), and a platinum counter electrode was used.

A standard procedure was adopted in acquiring the cyclic voltammograms to obtain good reproducibility of the data. The potentials were swept cyclically from hydrogen to oxygen evolution at a scan rate of 200 $mV\,s^{-1}$ until reproducible voltammograms were obtained (usually 10 min). With the same objective (reproducibility of the data) for impedance measurements in passivity, the Hastelloy C22 was prepassivated in the test solution at the temperature and measurement potential in potential steps upwards to higher passive potentials. After reaching current stability (a few minutes), the impedance measurements were carried out, and the potential was stable within 1 mV. In the passive–transpassive region, it was observed, following the suggestions of Bessone *et al.* [15], that the stationary conditions (characterized by a constant current) were achieved much faster during change of the potential towards a negative direction for samples which were already under stationary conditions. Thus, the impedance measurement sequence in the passive–transpassive region was: (1) to apply a given potential, say E, to achieve the corresponding stationary conditions (a few minutes), (2) to obtain its impedance spectrum (the impedance measurement took about 20 min) until reaching good reproducibility, (3) to shift the potential up to $E \pm \Delta E$ according to the passive or passive–transpassive potential and wait to ensure the new stationary condition, (4) to obtain the impedance spectrum at this new potential, and (5) to repeat the sequence from point 3 in the potential range. To minimize compositional changes caused by electrolysis in the oxide layer during impedance measurements, the frequency was scanned from high (100 kHz) to low (10 mHz) frequencies with an amplitude signal (potential signal) of $\pm$ 10 mV. The frequencies were scanned step by step with five steps per decade on a logarithmic scale. Two impedance measurements were carried out at each step and the spectra were judged to be satisfactory when they were identical over the whole frequency range. The Circelec and Casidie software programs written by Diard *et al.* [16, 17] were used to interpret the experimental impedance diagrams, making it possible to obtain values of the electrical circuit elements and kinetics at the electrode surface. The electrolyte after the tests was analysed using a Perkin–Elmer 3110 atomic absorption spectrometer (AAS) with continuum background correction (deuterium beam) and an HGA induction furnace with a pyro-coated graphite crucible. The detection limit of the AAS for each nickel, chromium,

TABLE I Composition of Hastelloy C22 steel

	Co	Cr	Fe	Ni	Mo	W
wt %	2.5	22	3	bal.	13	3

molybdenum, iron and cobalt main alloying elements at a signal-to-noise ratio of 3, was about 6×10^{-10} mol cm^{-3}. The sensitivity (quantification limit) which characterizes the variation of the value of optical density related to that of the alloying element concentration in the electrolyte, was found to be 3×10^{-10} mol cm^{-3}. The relative precision (relative standard deviation) of measurements obtained for several replicate determinations was about 3% (reproducibility). A linear calibration plot was obtained in the range from 2×10^{-9} to 5×10^{-8} mol cm^{-3}. After calibration by standard solutions, two sample measurements were carried out either with or without addition of standard solutions, because it is obvious that this procedure ensures elimination of any interference between the different alloying elements.

The composition of the Hastelloy C22 steel is given in Table I. This is a nickel-based alloy which has the feature that it contains cobalt. It should be noted that Hastelloy C22 is one of the stainless steels most resistant to corrosion, pitting and crevice formation [18].

3. Results and discussion

3.1. Anodic polarization curves

Fig. 1 shows the anodic and cathodic polarization curves obtained at a scan rate of 5 mV s^{-1} to study the corrosion of Hastelloy C22 steel at pH 3, over a temperature range of 20–70 °C. There is a slight shift of the corrosion potential, E_{corr}, towards the more positive potentials with increasing temperature. At this potential, the corrosion occurs as the result of cathodic and anodic reactions before the prepassivity.

The cathodic reactions can be written

$$A^+ + s + e^- \rightarrow A, s \quad (3)$$

$$A, s \rightarrow A + s \quad (4)$$

where A^+ and s are cathodic species and sites at the surface, respectively. Without any reducible species in solution, A^+ corresponds to H^+ at the acidic pH. The above cathodic reaction current is

$$i_c = -k_c F[A^+]^v \exp - FE/2RT \quad (5)$$

where k_c is the cathodic reaction rate constant and v the reaction order. For the anodic reaction, Hastelloy steel leads to $Me(OH)_{2ads}$ at the corrosion potential, E_{corr}, accordingly the reactions are

$$Me + H_2O \rightarrow MeOH_{ads} + H^+ + e^- \quad (6)$$

$$MeOH_{ads} + H_2O \rightarrow Me(OH)_{2ads} + H^+ + e^- \quad (7)$$

$$MeOH_{2ads} + H_2O \rightarrow Me(OH)_{3ads} + e^- \quad (8)$$

Equation 6 corresponds to the $Me(OH)_{ads}$ transient formation, and Equations 7 and 8 contribute to the passivity by means of $Me(OH)_{2ads}$ and Me_2O_3.

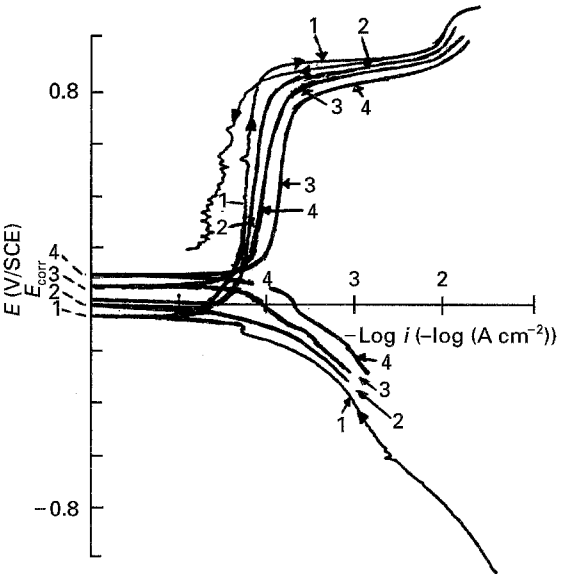

Figure 1 Polarization curves of Hastelloy C22 steel. Na_2SO_4 = 0.1 mol dm^{-3}; surface = 0.2 cm^2; scan rate = 5 mV s^{-1}; Ω = 3500 r.p.m.; pH = 3; temperature effect: (1) 20 °C, (2) 30 °C, (3) 50 °C, (4) 70 °C.

TABLE II Dependence of E_{corr} on temperature

T (°C)	E_{corr} (V/SCE)
20	− 0.075
30	− 0.05
50	0.04
70	0.1

The anodic reaction current at E_{corr} is equal to

$$i_a = 2k_a F[Me] \exp FE/RT \quad (9)$$

where k_a is the anodic rate constant.

At the corrosion potential, the anodic and cathodic currents are equal, and the behaviour of the corrosion potential with temperature may be derived from Equations 5 and 9, as was done by Jin Yun Zou and Der Tau Chin [19]. It is given by

$$E_{corr} = \frac{2.3\,RT}{1.5\,F}\left(\log\frac{k_c}{k_a} + v \log A^+\right) \quad (10)$$

According to Equation 10, plotting E_{corr} against T should give a straight line with a slope equal to

$$2.3R/1.5F\left(\log\frac{k_c}{k_a} + v \log A^+\right) \quad (11)$$

The experimental value found from Table II is 2 mV K^{-1}, which gives $k_a[A^+]^v/k_c = 1.5$; this value indicates that the corrosion potential increases with temperature.

As with Equation 10, the corrosion current is given by

$$i_{corr} = 1.26 k_a^{0.33} k_c^{0.66} F[A^+]^{0.66v} \quad (12)$$

From this equation, it appears that the corrosion current does not directly change with temperature. Effectively, the average experimental value of 0.25 μA cm^{-2} using the Tacussel software program

shows that the corrosion current does not change significantly with temperature. As shown in Fig. 1, increasing the temperature leads to a shift of the transpassive region towards less positive potentials. The shifts of corrosion potential and the transpassive region lead to a reduction of the passive region, as reported by Duquette *et al.* [20] for 316L stainless steel. The current instabilities during the backward scan in the passive region increase with lower passive potentials. These instabilities result from the fact that breakdowns of the passive oxide layer occur throughout this scan. In the transpassive peak, the backward scan current is higher than those in the forward scan for the same potential (curve 1). This behaviour is due to oxygen evolution and oxide dissolution through breakdowns of the passive layer according to Equation 13, where MeOOH is the hydrated oxide of Me_2O_3 on the surface.

$$MeOOH + 5OH^- \rightarrow MeO_4^{2-} + 3H_2O + 3e^- \quad (13)$$

3.2. Voltammetric curves

To elucidate the effect of temperature, it is worth observing the difference between polarization and voltammetric curves obtained at a high scan rate of 200 mV s^{-1}. In general, such curves may yield information on transient forms according to Equations 6–8 and as reported by Schrebler Guzman *et al.* [21], Sriram and Tromans [22] and Wieckowki *et al.* [23].

Fig. 2 shows the curves at pH 3, over a 20–80 °C temperature range with Hastelloy steel. A large prepassive peak is observed in this figure. This, which is set at 0.1 V/SCE for 20 °C, systematically increases with temperature. A negative shift of the peak potential as a function of the increase in temperature is observed, and the displacement is the reverse of the corrosion potential. The displacement can be attributed to the uncompensated ohmic drop and the kinetics of species formed in the active region. At higher temperature, the higher peak observed in the prepassive region, probably indicates a greater extent of species growth. The present results indicate that Hastelloy steel is more quickly corroded at higher temperature for the prepassive peak. At this scan rate, the passive region is not actually seen. Scan rate and temperature have a large effect on the kinetics of the oxide layer growth before and during stabilization in the active–passive region, and certainly the nature of the formed oxide layer may be different at low and high temperatures or scan rates. This dependence may reflect the effect of temperature on corrosion, as proposed by Jin You Zou and Der Tan Chim [24]. Beyond the short passive region, a considerable increase in current is observed, giving rise to a transpassive peak with adsorbate formation as hydroxide or adsorbed oxygen [25]; this peak increases with temperature. During the course of the backward scan, a reduction peak appears at − 0.8 V/SCE during the gradual increase in hydrogen evolution current; this reduction peak is conjugated to the prepassive peak.

To facilitate the selection of an active potential in order to obtain more accuracy for the spectroscopy impedance diagrams at different temperatures, the polarization curves with potentiostatic mode were plotted (Fig. 3). At 0.3 V/SCE, it is seen that the slope $\partial i/\partial E$ takes a negative value. This potential will be used to draw the impedance diagrams.

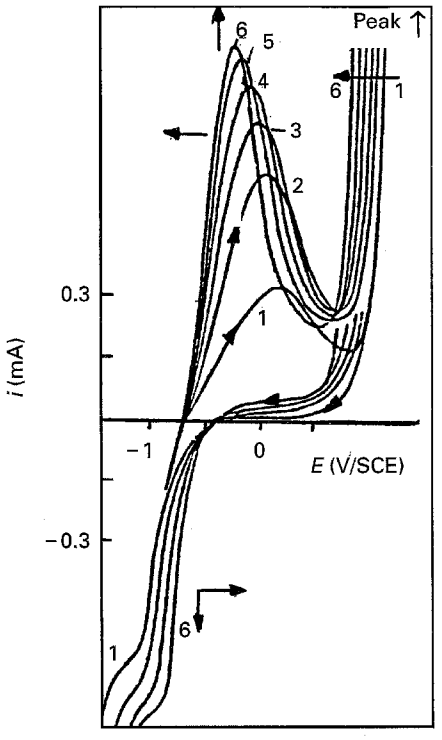

Figure 2 Voltammetric curves of Hastelloy C22 steel. Na_2SO_4 = 0.1 mol dm^{-3}; surface = 0.2 cm^2; scan rate = 200 mV s^{-1}; Ω = 2000 r.p.m.; pH = 3; temperature effect: (1) 20 °C, (2) 30 °C, (3) 40 °C, (4) 60 °C, (5) 70 °C, (6) 80 °C.

3.3. Impedance diagrams

The impedance diagrams were realized in the prepassivity, passivity and passivity–transpassivity limit.

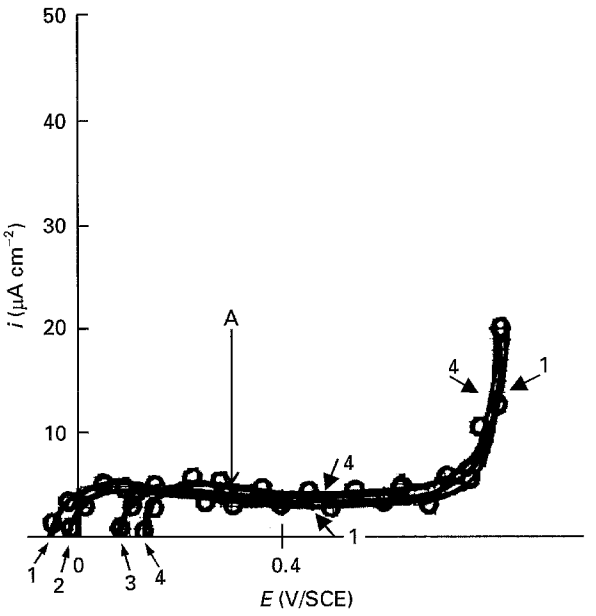

Figure 3 Potentiostatic mode polarization curves of Hastelloy C22 steel. Na_2SO_4 = 0.1 mol dm^{-3}; surface = 0.2 cm^2; Ω = 3500 r.p.m.; pH = 3; temperature effect: (1) 20 °C, (2) 30 °C, (3) 50 °C, (4) 70 °C.

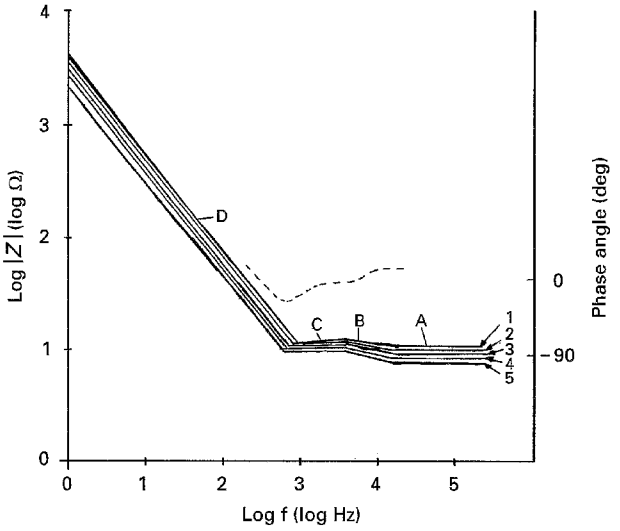

Figure 4 Electrochemical impedance spectroscopy, Bode diagrams in prepassivity. $Na_2SO_4 = 0.1$ mol dm^{-3}; surface = 0.2 cm^2; $\Omega = 0$ r.p.m.; pH = 3; $E = 0.3$ V/SCE; temperature effect: (1) 20 °C, (2) 30 °C, (3) 40 °C, (4) 60 °C, (5) 70 °C, (– – –) phase angle.

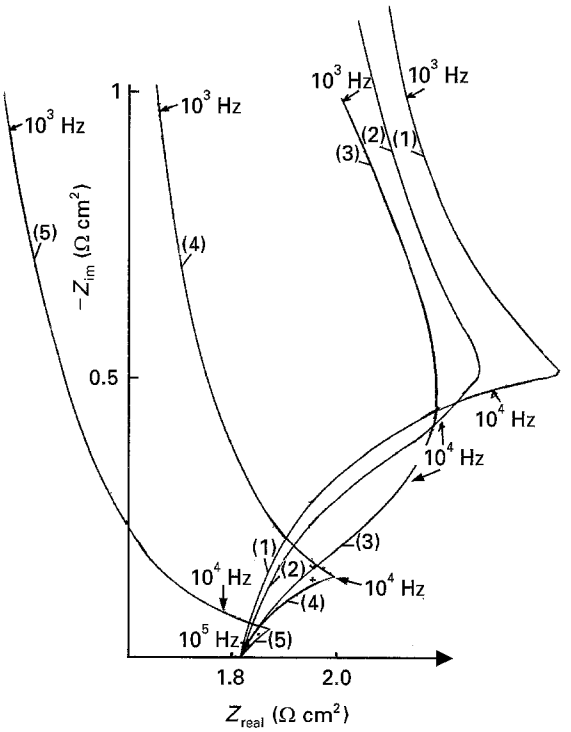

Figure 5 Impedance diagrams of Hastelloy C22 steel, Nyquist diagrams in prepassivity. $Na_2SO_4 = 1$ mol dm^{-3}; surface = 0.2 cm^2; $\Omega = 0$ r.p.m.; pH = 3; $E = 0.3$ V/SCE; temperature effect: (1) 20 °C, (2) 30 °C, (3) 40 °C, (4) 60 °C, (5) 70 °C.

The potentials in prepassivity were selected with respect to the polarization curves drawn with the potentiostatic mode (Fig. 3), where the current slightly decreases after the active peak. Fig. 4 shows the Bode plots of the passive oxide layer formation of 0.3 V/SCE (point A in Fig. 3) for different temperatures. From the interpretation of Gebhardt [26], the impedance spectra can be analysed as follows. Segment A is characterized by the electrolyte resistance at the highest frequencies. Segment B appears when the frequency decreases, and the electrical response is the impedance of the oxide marked by non-dispersive characteristics. The slope of segment B may be -1, and in our case the very small slope may be attributed to the superposition of the real impedance. At lower frequencies, segment C appears and the slope is nil instead of -0.2 to -0.3; the real impedance may again play a role here. Segment D is characterized by a long straight line with a slope of about -1, and would appear to correspond here to a capacitive branch which tends towards infinite imaginary impedance in a Nyquist plot; a more compact oxide is formed. With respect to Segment B, it is difficult to calculate the thickness of non-dissipative insulating oxide formed, as indicated by Gebhardt [26] and Castro and Vilche [27], therefore we have drawn the experimental Nyquist diagrams (Fig. 5) using a lower electrolytic resistance. These diagrams are formed of a capacitive semi-circle at higher frequencies, followed by capacitive branches that tend towards infinity from the semi-circle down to 0.01 Hz, meaning passivity. At higher frequencies, even at 10^4 Hz, the overlapped capacitive semi-circle can be interpreted by the growth of the passive layer. With increasing temperature, the semi-circles are much lower, meaning a higher oxide layer growth and these are hidden by the capacitive branch, which is linked to segment B. As regards the semi-circle obtained at higher frequencies, we have calculated the capacitance, C, from $C = (2\pi fZ)^{-1}$, where f is the frequency taken at the top of semi-circle, and Z is the real impedance of the semi-circle.

The thickness of the insulating oxide for a plane area can be obtained from

$$l = \varepsilon\varepsilon_0 r\, A/C \qquad (14)$$

where l denotes the thickness of the insulating oxide, A the area, ε and ε_0 the relative and absolute (vacuum permittivity) dielectric constants, respectively. From the Handbook of Chemistry and Physics values, the absolute dielectric constant (ε_0) is 9×10^{-14} F cm^{-1}, as indicated by Simoes *et al.* [28], Curley-Fiorino and Schmid [29], Rak-Hyun Song *et al.* [30], and Moffat and Latanision [31]. The relative dielectric constant, ε, of oxide generally varies over 5–25, for example, the value would be 16 for a passive layer on AISI 304 stainless steel [28, 29], 14 for Fe_2O_3 [30], and 25 for Cr_2O_3 [31]; these are the major oxides leading to the passivity of steel. As the relative dielectric constant, ε, for Hastelloy was not found in the literature, we have measured the current with time during potentiostatic oxide formation at 0.3 V/SCE (Fig. 6). Under potentiostatic conditions, the current response may be attributed to two possible processes: passive layer formation and oxide layer dissolution. Thus, we have quantitatively analysed the electrolyte by atomic absorption spectrometry (AAS); before analysis, the potential was held for 1 h at 0.3 V/SCE. Taking a pyro-coated graphite crucible, the detection limit by AAS was found to be 6×10^{-10} mol cm^{-3} per metal cation, while the total amount of oxide was calculated from Fig. 12 (see later) to be 2×10^{-8} mol taking a surface of 1 cm^2 in tests. The double-layer charging current should be negligible (no greater than 15 μA at passive potentials). The method therefore is suitable for showing some metallic cations in electrolytes. The amounts of iron, nickel and chromium analysed in the

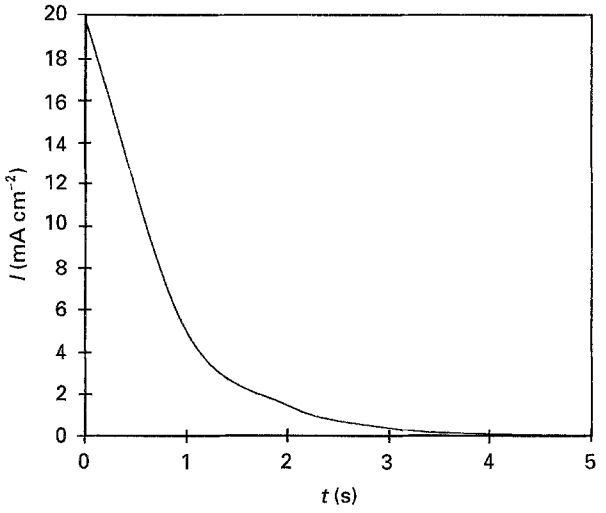

Figure 6 Current as a function of time in passivity.

electrolyte were negligible. Therefore, the quantity of the total charge obtained integrating the current–time curve in Fig. 6, corresponds to the oxide layer formation. According to Faraday's law, the oxide layer thickness, l, can also be calculated from

$$l = QM/nF\rho r \qquad (15)$$

where M is the mean molar weight of oxide, assumed to be about 159, and ρ the oxide density equal to 5.2 g cm^{-3}, according to Schmuki and Böhni [32] and MacDonald and Roberts [33], and n the mean number of electrons required to form the passive oxide. Substitution of Equation 14 into Equation 15 therefore yields the value of ε and the result found is 20. The thickness values from Equation 14, are given in Table III. Apparently these decrease with temperature.

On drawing the Bode diagrams between -0.5 V/SCE and 0.6 V/SCE, the segment D is obtained as in Fig. 4. These diagrams allow us to calculate the donor or acceptor concentration following Equation 16

$$C^{-2} = \frac{2kT}{e\varepsilon\varepsilon_0 r n_d}(V_m - V_{fb} - kT/e) \qquad (16)$$

where e is the charge of the electron, n_d the donor density, and V_m, V_{fb} the potentials at which the impedance measurements are carried out and the flatband potential, respectively. The results are given in Fig. 7; linearity is observed between 0 and 0.2 V/SCE, and using Equation 16, the donor density is calculated from the slope of the linear region; this is 4.9×10^{20} carriers cm^{-3}. The flatband extrapolated potential is close to -0.3 V/SCE. The carrier concentration is in agreement with the theoretical value for a passive layer given by Castro and Vilche [27], Simoes *et al.* [28] and Rak-Hyun Song *et al.* [30].

The Nyquist plots obtained at higher potentials than those of prepassivity and for different temperatures are shown in Fig. 8. These diagrams are completely different from those obtained for the prepassivity and they are formed only of a capacitive semi-circle. It is observed that the size of capacitive semi-circle decreases when the potentials or temperature increase, signifying more corrosion.

TABLE III Dependence of thickness on temperature at 0.3 V/SCE

	T(°C)				
	20	30	40	60	70
e (nm)	0.5	0.4	0.3	0.2	0.2

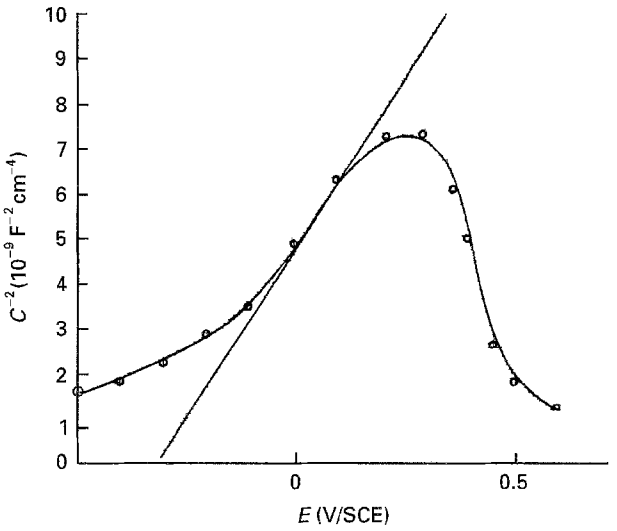

Figure 7 Mott-Schottky plots of passive layer Na_2SO_4 = 1 mol dm^{-3}; surface = 0.2 cm^2; Ω = 0 r.p.m.; pH = 3; temperature: 20 °C.

The impedance diagrams obtained at the passivity–transpassivity limit potentials are shown for different temperatures in Fig. 9. The Nyquist response is well represented by a capacitive semi-circle and inductive loop which corresponds to an adsorption phenomenon leading to a secondary passivity in the transpassive peak region, as indicated by Magaino *et al.* [34], Epelboin and Keddam [35], Feller *et al.* [36], Jouanneau *et al.* [37] and Gebhardt [26]. The interpretation of the capacitive semi-circle with the centre slightly below the real axis could be that the dissolution by formation of FeO_4^{2-}, CrO_4^{2-}, MoO_4^{2-} through breakdown of the passive oxide is limited by the adsorption. As the temperature increases, the size of the semi-circle decreases; this is the result of the oxidation current increasing, leading to the dissolution of the oxide layer. The small size of the semi-circle indicates that Hastelloy steel is easily corroded at the passivity–transpassivity limit potential and this is also shown by the pink colour of the electrolyte, signifying the presence of cobalt ions. Therefore, the electrolyte used was analysed for iron, chromium, nickel and cobalt ions by the atomic absorption spectrometer with an HGA induction furnace at 2700 °C. The calibrations were made with Co^{2+}, Ni^{2+}, Cr^{6+}, Fe^{2+} and Mo^{6+} solutions at concentrations between 2×10^{-9} and 5×10^{-8} mol cm^{-3} for each ion and pH 3; the wavelengths were, respectively, 240.7, 232.0, 357.9, 248.3 and 240.7 nm. The electrolyte analysis results are given in Table IV. In comparison with Table I, these show a selective corrosion of cobalt and an enrichment of chromium and molybdenum on the surface of Hastelloy.

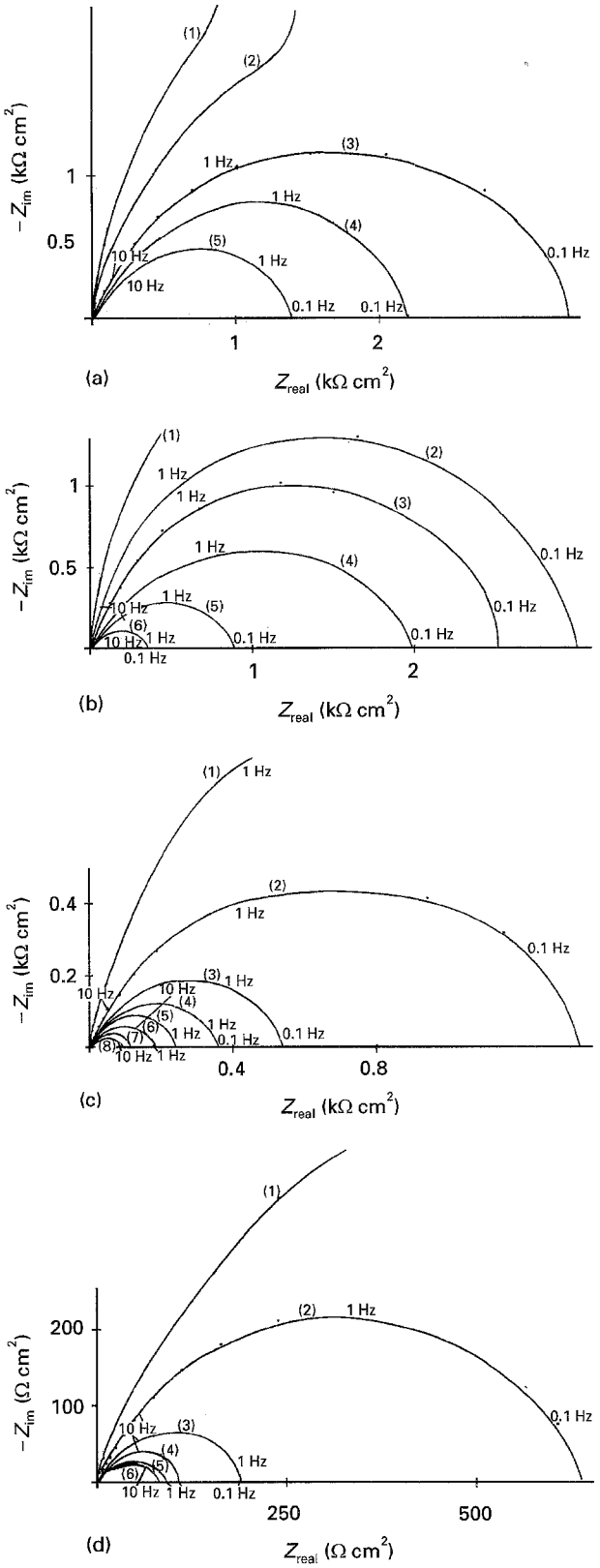

Figure 8 Experimental and simulated impedance diagrams of Hastelloy C22 steel, Nyquist diagrams in passivity. Na_2SO_4 = 0.1 mol dm^{-3}; surface = 0.2 cm^2; Ω = 0 r.p.m.; pH = 3. (a) 20 °C, potentials: (1) 0.5, (2) 0.6, (3) 0.7, (4) 0.75, (5) 0.8 V/SCE. (b) 40 °C, potentials: (1) 0.4, (2) 0.5, (3) 0.6, (4) 0.7, (5) 0.75, (6) 0.8 V/SCE. (c) 60 °C, potentials: (1) 0.4, (2) 0.5, (3) 0.6, (4) 0.62, (5) 0.65, (6) 0.7, (7) 0.75, (8) 0.8 V/SCE. (d) 80 °C, potentials: (1) 0.4, (2) 0.5, (3) 0.6, (4) 0.7, (5) 0.75, (6) 0.8 V/SCE.

Previous studies of passive oxide layers formed from nickel-based superalloys have involved techniques such as secondary ion mass spectrometry (SIMS), X-ray photoelectron spectroscopy (XPS) as

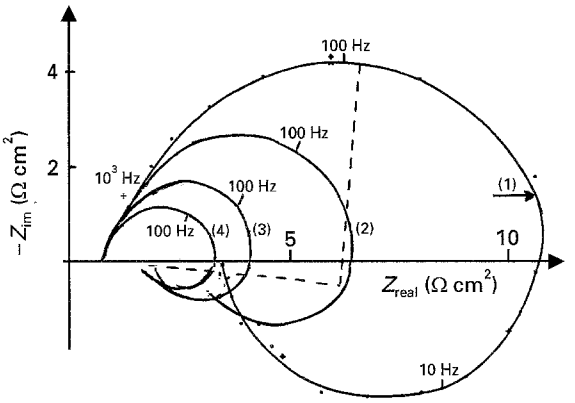

Figure 9 Experimental and simulated impedance diagrams of Hastelloy C22 steel, Nyquist diagrams in passivity–transpassivity limit. Na_2SO_4 = 1 mol dm^{-3}; surface = 0.2 cm^2; pH = 3; E = 0.9 V/SCE; temperature effect: (1) 20 °C, (2) 30 °C, (3) 40 °C, (4) 60 °C.

TABLE IV Composition of electrolyte after corrosion of Hastelloy

	Co	Cr	Fe	Ni	Mo
wt %	23	12	3	56	6

well as Auger electron spectroscopy (AES), and surface analysis by laser ionization (SALI). SIMS is sensitive to matrix effects. As a result, calibration with standards of similar structure and composition is required to determine quantitatively the composition of the sample, but such standards are usually inappropriate for very thin oxide layers. AES and XPS are much more quantitative than SIMS, but their sensitivity is rather limited. In contrast, SALI has the capability of performing in depth and laterally resolved chemical composition measurements quantitatively and with a sensitivity comparable to that of SIMS, but without being greatly susceptible to matrix effects. The depth resolution and detection limits for SALI exceed those for AES and XPS. From Pound and Becker's results [38] using the SALI technique for a nickel-based superalloy containing cobalt, the oxide layer is basically $(Ni_{0.3}Co_{0.02}Cr_{0.5}Mo_{0.16}Fe_{0.02})_xO_y^{2-}$. The oxide layer formed is characterized by a higher chromium content due to the marked segregation of this element to the oxide layer which appears to be a general phenomenon for passive oxide layers. This enrichment was accompanied by a depletion in nickel, and it was found that the molybdenum content of the passive layer is slightly enriched. From Pound and Becker's studies [38], AES also indicates that molybdenum was midway through the oxide layer but not on the surface or in the near surface layer. The combination of a higher chromium and slightly higher molybdenum content in the oxide on nickel-based superalloy containing cobalt would be expected to render this alloy extremely corrosion resistant, which was in fact observed experimentally in our laboratory [39, 40]. In the same way, the studies of Olefjord [41] give a duplex structure of the passive layer with an outer layer of hydrated hydroxide and an inner layer of oxide. The inner is at least two thirds of the total oxide

with an appropriate localization of alloying elements in a spinel lattice.

4. Discussion equivalent circuits and value determination

The experimental impedance diagrams obtained in the active, passive and transpassive regions and for different temperatures are complex and show that the equivalent circuits to be analysed are evolutive. From the experimental diagrams and each proposed equivalent circuit, it is possible to plot simulated impedance diagrams which must have the same characteristics as the previous diagrams, i.e. the same shape and real and imaginary impedance values and also the same position and frequency shifts. These allow the values of electrical elements to be obtained.

Before giving the equivalent circuit for the active region, the experimental diagrams with the real and imaginary impedances, which tend towards the negative and infinite values, respectively, are interpreted below following the explanations given by Epelboin *et al.* [42] and Jouanneau *et al.* [37].

According to Epelboin, the faradaic impedance is dependent on

$$1/Z_F = 1/R_{ct} + f'_E b/(j\omega - a) \quad (17)$$

where R_{ct} is the charge transfer resistance, $f'_E = (\partial i/\partial E)_x$ is the ratio of the current to potential variations in the prepassive region, x a parameter depending on adsorbates (Equations 6–8), which depend on temperature [43], ω the angular frequency and a is related to

$$a = \tau_x^{-1} \quad (18)$$

where τ_x is the time constant related to the parameter x. In the same way as a, the term b depends on the active potentials time constant. From Equation 17, for a sufficiently high frequency with $\omega \gg \tau_x^{-1}$, the expression $f'_E b/(j\omega - a)$ tends to zero, therefore we have

$$(1/Z_F)_{f\to\infty} = 1/R_{ct} \quad (19)$$

At lower frequencies, with $\omega \ll \tau_x^{-1}$, the current follows the variation of the parameter depending on adsorbates, which depend on the temperature, and Equation 17 becomes:

$$(1/Z_F)_{f\to 0} = 1/R_{ct} - f'_E b/a = 1/R_p \quad (20)$$

where R_p is the polarization resistance. With respect to the curves in Fig. 3, the point A gives a slight negative slope of $\partial i/\partial E$, compatible with the polarization resistance variation, which enables us to conclude that the term $f'_E b/a$ in Equation 17, tends to increase the impedance value towards infinity, and then to shift the spectrum towards the negative real part at lower frequencies, depending on the temperature. The shape of these impedance diagrams is characteristic of the active region and passivating process in accordance with Jounneau *et al.*'s results [37].

The diagrams obtained for the prepassive regions (Figs 4 and 5) should be satisfactorily explained on the basis of the equivalent circuit presented in Fig. 10. In this, the R_{el} term is the electrolytic resistance, C_{dl} reflects double-layer capacitance, C_{ox}, R_{ox} are the passive oxide formation capacitance and resistance, R_p the polarization resistance and W is a Warburg impedance. One of the aims of plotting the experiment diagrams is to find the values of the main electric elements using the Circelec software program. Fo this, in the simulated Nyquist diagrams (Fig. 11), th size, the shape of the semi-circle, the part which tend towards the negative, infinite real and imaginary im pedances and position of the frequencies coincide wit the experimental Nyquist diagrams given as a functio of temperature (Fig. 5). The values obtained for th electrical elements are given in Table V; the electro lytic resistance is about $2\,\Omega\,cm^2$, the experimenta double-layer capacitance value is estimated to b $25\,\mu F\,cm^{-2}$ at the corrosion potential; this value slightly higher ($50\,\mu F\,cm^{-2}$) in the active regio These values of the double-layer capacitance corre

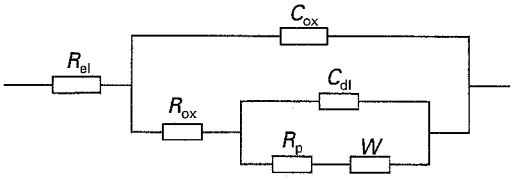

Figure 10 Equivalent circuit for impedance simulation followi Figs 4 and 5. R_{el} = electrolyte resistance, R_{ox} = oxide formatic resistance, C_{ox} = oxide formation capacitance, R_p = polarizatic resistance, C_{dl} = double-layer capacitance, W = Warburg coefficier

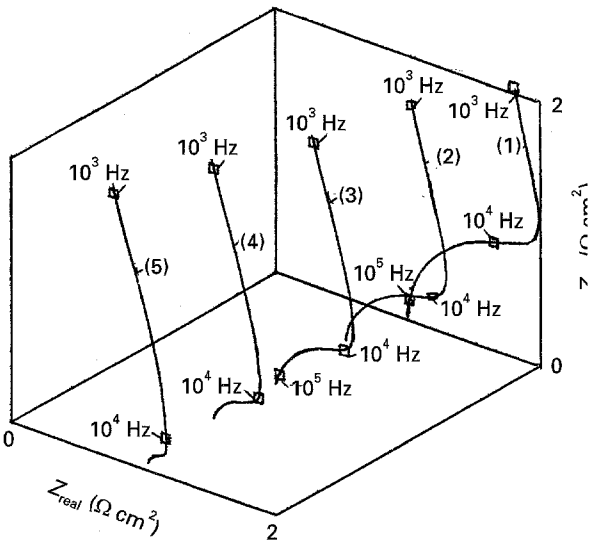

Figure 11 Simulated impedance diagrams for comparison wi Fig. 5. $Na_2SO_4 = 1$ mol dm^{-3}; surface = 0.2 cm^2; $\Omega = 0$ r.p.m pH = 3; $E = 0.3$ V/SCE; temperature effect: (1) 20 °C, (2) 30 ° (3) 40 °C, (4) 60 °C, (5) 70 °C. Parameter values are given Table V.

TABLE V Effect of temperature in the prepassive regic ($E = 0.3$ V/SCE)

	T (°C)				
	20	30	40	60	70
R_{el} ($\Omega\,cm^2$)	2.2	2.0	1.9	1.9	1.7
R_{ox} ($\Omega\,cm^2$)	1.6	1.3	1	0.5	0.2
C_{ox} (10^{-5} F cm^{-2})	2	1.7	1.5	1.2	1
C_{dl} (10^{-5} F cm^{-2})	4.5	4.5	5	5.2	5.5
W ($\Omega\,cm^2\,s^{-0.5}$)	410	400	400	390	395

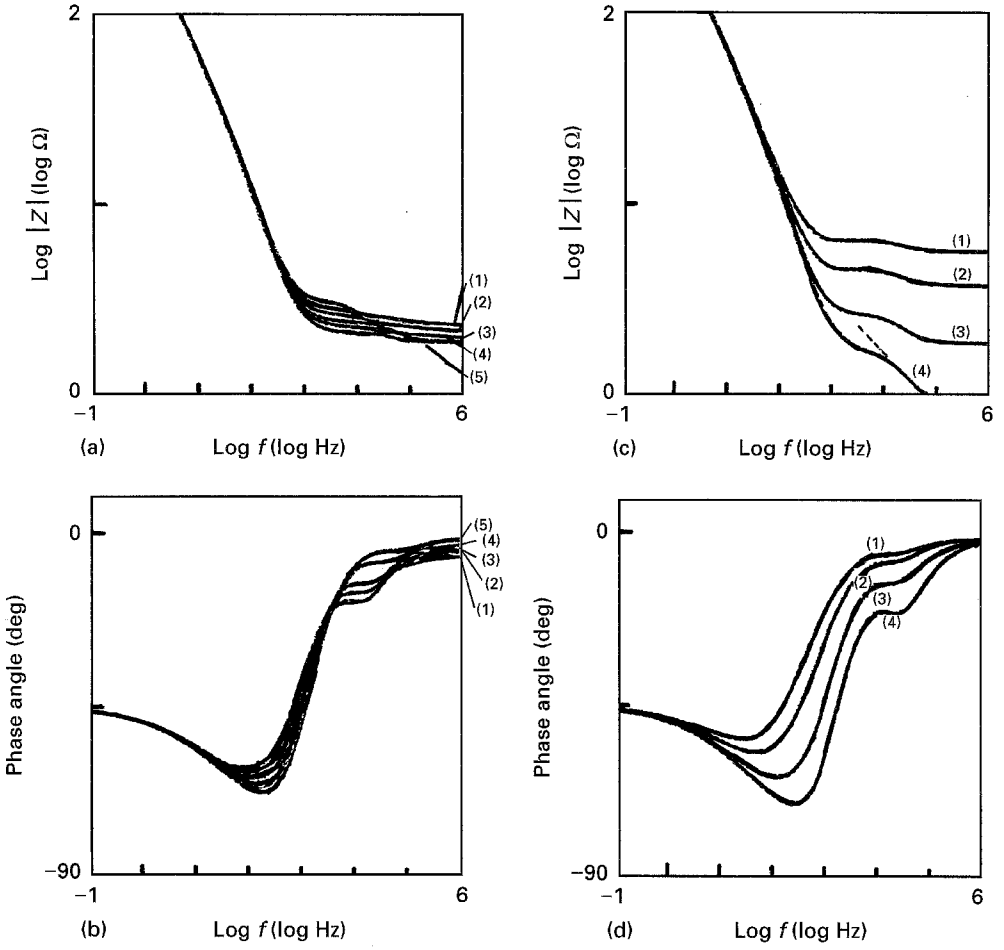

Figure 12 Simulated impedance diagrams for comparison with Fig. 4 (impedance and phase angle). $Na_2SO_4 = 0.1\ mol\ dm^{-3}$; surface $= 0.2\ cm^2$; $\Omega = 0$ r.p.m.; pH = 3; $E = 0.3$ V/SCE; temperature effect: (a, b) $R_{el} = 6\ \Omega cm^2$, (1) 20 °C, (2) 30 °C, (3) 40 °C, (4) 60 °C, (5) 70 °C; (c, d) 20 °C, (1) $R_{el} = 6\ \Omega cm^2$, (2) $R_{el} = 4\ \Omega cm^2$, (3) $R_{el} = 2\ \Omega cm^2$, (4) $R_{el} = 1\ \Omega cm^2$.

pond to a normal value according to Bard and Faulkner [44]. From Table V, the oxide capacitance value is $10\ \mu F\ cm^{-2}$ and represents a characteristic oxide. The oxide and double-layer capacitance value indicate the passivity of Hastelloy.

In the impedance diagrams realized at different temperatures for 0.3 V/SCE and from the equivalent circuit results, the overlapped capacitive semi-circle at the high frequencies, even at 10^4 Hz, is due to the growth of passive oxide characterized by C_{ox} and R_{ox}. In addition to the capacitive semi-circle, the part at lower frequencies, which tends towards the negative real impedance corresponds to the previous explanations given by Epelboin for the negative $\partial i/\partial E$ slope obtained at the point A in Fig. 3, and corresponds to the double-layer capacitance, C_{dl}, in parallel with a negative polarization resistance, R_p, and Warburg impedance, W, in the equivalent circuit. The passive oxide formation resistance values are small and decrease slightly when the temperature increases, signifying a slight enhancement of oxide formation.

In the Bode diagrams (Fig. 4), R_{el} and R_{ox} are equal to 6 and 1 Ωcm^2, respectively. The accurate measurement of oxide thickness appears to be difficult in the simulated plot (Fig. 12a, b), due to the low value of R_{ox} with respect to R_{el}, and consequently it impedes the appearance of the phase angle and the second impedance slope of about -1 in the region B (Fig. 4). It is nevertheless, possible to calculate the value of

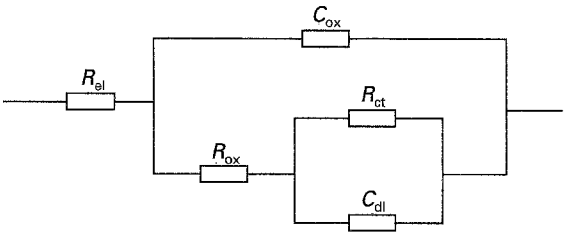

Figure 13 Equivalent circuit for impedance simulation following Fig. 7. R_{el} = electrolyte resistance, R_{ox} = oxide formation resistance, C_{ox} = oxide formation capacitance, R_{ct} = charge transfer resistance, C_{dl} = double layer capacitance.

oxide formation taking into account the value of the electrolytic resistance. On this basis, we have redrawn the diagram (Fig. 12c, d) with a lower value of R_{el} ($1\ \Omega cm^2$) and using the Circelec software program written by Diard *et al.* [16, 17]. The modules show the phase angle and two very well-defined slopes equal to -0.5 at lower frequencies and -1 at higher frequencies in which it is possible to measure C_{ox}, and therefore Equation 14 allows us to determine the oxide thickness. This is about a few Angströms and as in the previous results, the thickness of the passive oxide is the lowest for higher temperatures.

In the case of passivity, the experimental diagrams in Fig. 8, can be explained by the equivalent circuit presented in Fig. 13. In this circuit, the terms C_{ox} and R_{ox} can be neglected in comparison to values of

TABLE VI Effect of temperature in the passive region and for different potentials at 20 and 40 °C

T (°C)		E (V/SCE)						
		0.4	0.5	0.6	0.62	0.7	0.75	0.8
20	R_{el} (Ω cm^2)	–	–	–	–	1.7	1.7	1.65
	R_{ct} (Ω cm^2)	–	–	–	–	2970	2100	1400
	C_{dl} (10^{-4} F cm^{-2})	–	–	–	–	2	1.5	1
40	R_{el} (Ω cm^2)	–	1.5	1.5	–	1.5	1.45	1.45
	R_{ct} (Ω cm^2)	–	2750	2450	–	1700	1050	400
	C_{dl} (10^{-4} F cm^{-2})	–	2	1.7	–	1.5	1.2	1
60	R_{el} (Ω cm^2)	–	–	1.3	1.3	1.25	1.25	1.2
	R_{ct} (Ω cm^2)	–	–	550	420	180	100	90
	C_{dl} (10^{-4} F cm^{-2})	–	–	2	1.7	1.5	1.3	1
80	R_{el} (Ω cm^2)	1.1	1.1	1.1	–	1.05	1.05	1
	R_{ct} (Ω cm^2)	1400	500	300	–	95	80	75
	C_{dl} (10^{-4} F cm^{-2})	2	1.8	1.6	–	1.5	1.3	1.2

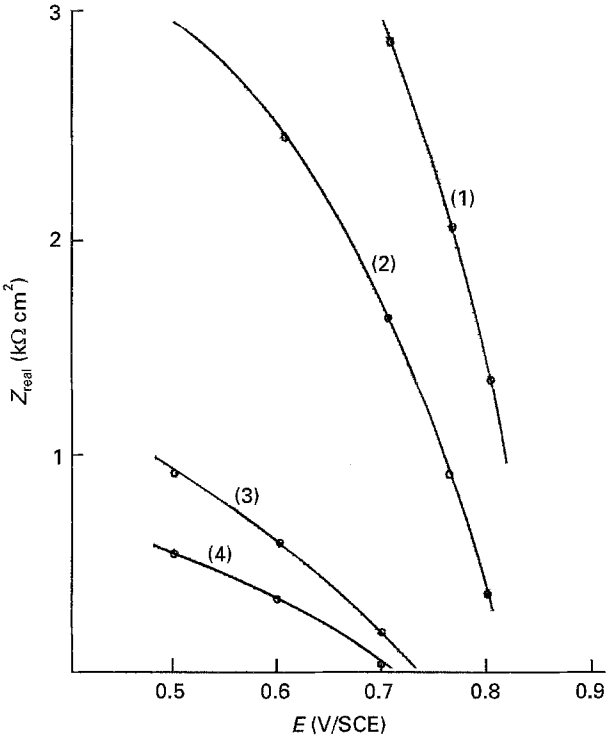

Figure 14 Charge-transfer resistance as a function of passive potentials and temperature, following Fig. 13. (1) 20 °C, (2) 40 °C, (3) 60 °C, (4) 80 °C.

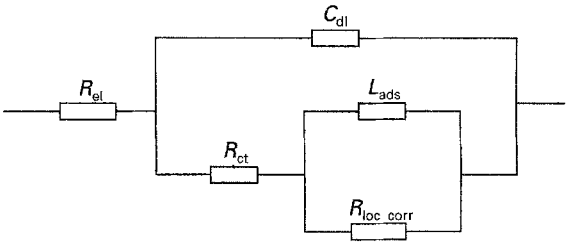

Figure 15 Equivalent circuit for impedance simulation following Fig. 8. R_{el} = electrolyte resistance, $R_{loc,corr}$ = localized corrosion resistance, L_{ads} = adsorption inductance, R_{ct} = charge-transfer resistance, C_{dl} = double layer capacitance.

R_{ct} corresponding to the passivity. In the simulated Nyquist diagrams obtained from the equivalent circuit, the size, shape of semi-circle and shifts of the frequencies coincide exactly with the experimental diagrams (Fig. 8). The values of the electrical elements using the Circelec software program are given in Table VI. From this, it is observed that the charge-transfer resistance decreases (Fig. 14) when the potentials or temperature increase, signifying more corrosion. Taking the average value of 150 μF cm^{-2} (corresponding to Fig. 8), from the Casidie program applied to passivity and dissolution mechanisms, and written by Diard *et al.* [16, 17], the average rate constant is 10^{-2} mol cm^{-2} s^{-1}, and the number of active sites is 10^{-10} mol cm^{-2} for a potential near the passivity, and 3×10^{-8} mol cm^{-2} for a potential near the passivity–transpassivity limit. The rate constant value is low and shows that Hastelloy is slightly corroded at these potentials. The increase in the number of active sites at the passivity–transpassivity limit indicates that the passive oxide starts to break down.

The experimental diagrams (Fig. 9) obtained at the passivity–transpassivity limit and different temperatures can be satisfactorily explained on the basis of an equivalent circuit (Fig. 15). The faradaic impedance implies the charge-transfer resistance in series with an inductance, in parallel with localized corrosion resistance. From these, the faradaic impedance is given by

$$Z_F = R_{ct} + \frac{j\omega L_{ads} R_{loccorr}}{R_{loccorr} + j\omega L_{ads}} \quad (21)$$

From this equation, the faradaic impedance includes the charge transfer, R_{ct}, and localized corrosion, $R_{loccorr}$, resistances, and the adsorption inductance, L_{ads}. We drew the simulated diagrams which coincide exactly with the experimental diagrams with respect to the temperature for a constant potential, to ascertain the suitable electrical elements using the Circelec software program. It is found that the diameter of the capacitive semi-circle, the inductive loop and the phase angle decrease when the temperature increases, indicating corrosion enhancement and a decrease in adsorption. The values of the equivalent circuit elements are given in Table VII. As the temperature increases, the charge-transfer and localized corrosion

TABLE VII Effect of temperature in the passivity–transpassivity limit

	T (°C)			
	20	40	60	70
R_{el} (Ω cm^2)	1.4	1.35	1.3	1.2
C_{dl} (10^{-4} F cm^{-2})	1.6	1.4	1.3	1.2
R_{ct} (Ω cm^2)	5	3	3	2.5
L_{ads} (H cm^2)	0.2	0.18	0.2	0.22
$R_{loc\,corr}$ (Ω cm^2)	11	8	4.2	3.7

resistances decrease; this is the result of the oxidation current increasing. Taking the average value of 150 μF cm^{-2} (corresponding to Fig. 9), from the Casidie program for passivity and dissolution mechanisms written by Diard *et al.* [16, 17], the average rate constants is 0.1 mol cm^{-2} s^{-1} and the number of active sites is between 2 and 9×10^{-6} mol cm^{-2}. These increase with temperature and potentials.

5. Conclusion

The polarization curves show that the corrosion potential of Hastelloy C22 steel increases with increasing temperature. Increasing the temperature leads to a shift of the transpassive region towards less positive potentials. These lead to a reduction of the passive region. The current instabilities during the backward scan and the higher current than that in the forward scan show that all the oxide layer would not be destroyed at a high transpassive potential in the backward scan. An intermediate peak is found by voltammetry in the prepassive region; its current increases with temperature. In contrast to the corrosion potential, the intermediate peak potential shifts towards more negative values with increasing temperature. These results indicate that Hastelloy steel is more quickly corroded at a higher temperature in the prepassive region. From electrochemical impedance spectroscopy, apparently the thickness of passive oxide decreases with temperature. The donor concentration was calculated, and the value obtained for 20 °C is in agreement with theoretical value for a passive layer.

In the passivity, the size of the capacitive semi-circle is large. This decreases with an increase in the passive potentials and temperature, signifying corrosion enhancement. The number of active sites and the oxidation rate constant were determined.

At the passivity–transpassivity limit potentials, using impedance spectroscopy, an inductive loop may be the result of adsorption. It is found that the diameter of the capacitive semi-circle and the inductive loop decrease when the temperature increases, indicating corrosion enhancement and a decrease in adsorption. The equivalent circuits and the values of elements were determined in the prepassivity, passivity and passivity–transpassivity limits.

References

1. G. BELLANGER and J. J. RAMEAU, *Corros. Sci.* **36** (1994) 545.
2. G. BELLANGER, *J. Nucl. Mater.* **210** (1194) 63.
3. A. ROUSTILA, N. KUROMOTO, A. M. BRASS and J. CHÊNE, *J. Nucl. Mater.* **211** (1994) 156.
4. A. M. BRASS, J. CHÊNE and J. GONZALEZ, *Metal. Mater. Trans.* **25A** (1994) 1159.
5. A. BRUGGEMAN, M. SNYKERS and P. de REGGE, *Fusion Technol.* **14** (1988) 828.
6. W. G. BURNS and P. B. MOORE, *Rad. Effects* **30** (1976) 233.
7. J. K. LINACRE and W. R. MARSH, report R 10027, Chemistry Division, Atomic Energy Research Establishment, Harwell, UK (1981).
8. J. WRIGHT, J. K. LINACRE, W. R. MARSH and T. R. BATES, in "Proceedings of the International Conference on the Peaceful Uses of Atomic Energy", Vol. 7, 8–20 August 1955 ed. United Nations (United Nations, New York, 1956) p. 560.
9. V. A. MACAGNO and J. W. SCHULTZE, *J. Electroanal. Chem.* **180** (1984) 157.
10. J. W. SCHULTZE and V. A. MACAGNO, *Electrochim. Acta* **31** (1986) 355.
11. L. YOUNG, "Anodic Oxide Film" (Academic Press, London, 1961).
12. O. KERREC, D. DEVILLIERS, C. HINNEN and P. MARCUS, in "Symposium on Modifications of Passive Films", ed. EFC (European Federation of Corrosion, London, 1994) p. 206.
13. O. KERREC, Thesis, Paris (1992).
14. W. WILHELMSEN, *Electrochim. Acta* **33** (1988) 63.
15. J. B. BESSONE, D. R. SALINAS, C. E. MAYER, M. EBERT and W. J. LORENZ, *ibid.* **37** (1992) 2283.
16. J. P. DIARD, P. LANDAUD, B. LE GORREC and C. MONTELLA, in "Deuxième Forum sur les Impedances Electrochimiques", Montrouge, France ed. Gabrielli (University of Paris, Jussieu, 1987).
17. J. P. DIARD, B. LE GORREC and S. MAXIMOVITCH, *Electrochim. Acta* **35** (1990) 6.
18. A. J. SEDRIKS, "Corrosion of Stainless Steels" (Wiley, New York, 1979).
19. JIN YUN ZOU and DER TAU CHIN, *Electrochim. Acta* **32** (1987) 1751.
20. D. J. DUQUETTE, K. L. WRISLEY, E. COOMER and D. STEINER, *J. Nucl. Mater.* **194** (1992) 992.
21. R. S. SCHREBLER GUZMAN, J. R. VILCHE and A. J. ARVIA, *J. Appl. Electrochem.* **11** (1981) 551.
22. R. SRIRAM and D. TROMANS, *Corros. Sci.* **25** (1985) 79.
23. A. WIECKOWSKI, E. GHALI and HUY HA LE, *J. Electrochem. Soc.* **131** (1984) 9.
24. JIN YOU ZOU and DER TAU CHIN, *Electrochim. Acta* **33** (1988) 447.
25. M. R. TARASEVICH, A. SADKOWSKI and E. YEAGER, in "Comprehensive Treatise of Electrochemistry", Vol. 7, "Kinetics and Mechanisms of Electrode Processes", edited by J. O' M. Bockris, B. E. Conway, E. Yeager and R. E. White (Plenum Press, New York, 1983).
26. O. GEBHARDT, *Electrochim. Acta* **38** (1993) 633.
27. E. B. CASTRO and J. R. VILCHE, *ibid.* **38** (1993) 1567.
28. A. M. P. SIMOES, M. G. S. FERREIRA, B. RONDOT and M. DA CUNHA BELO, *J. Electrochem. Soc.* **137** (1990) 1.
29. M. E. CURLEY-FIORINO and G. M. SCHMID, *Corros. Sci.* **20** (1980) 313.
30. RAK-HYUN SONG, SU-IL PYUN and R. A. ORIANI, *J. Appl. Electrochem.* **21** (1991) 181.
31. T. P. MOFFAT and R. M. LATANISION, *J. Electrochem. Soc.* **139** (1992) 7.
32. P. SCHMUKI and H. BÖHNI, *Electrochim. Acta* **40** (1995) 775.
33. D. D. MACDONALD and B. ROBERTS, *ibid.* **23** (1978) 781.
34. S. MAGAINO, M. MATLOSZ and D. LANDOLT, *J. Electrochem. Soc.* **140** (1993) 5.
35. I. EPELBOIN and M. KEDDAM, *Electrochim. Acta* **17** (1972) 177.
36. H. G. FELLER, H. J. RATZER-SCHEIBE and W. WENDT, *ibid.* **17** (1972) 187.
37. A. JOUANNEAU, M. KEDDAM and M. C. PETIT, *ibid.* **21** (1976) 287.
38. B. C. POUND and C. H. BECKER, *J. Electrochem. Soc.* **138** (1991) 696.

39. G. BELLANGER, CEA-R 5664 report, edited by C. E. Saclay, Gif sur Yvette, France (1994).
40. *idem*, CEA-R 5665 report, edited by C. E. Saclay, Gif sur Yvette, France (1994).
41. I. OLEFJORD, B. BROX and U. JELVESTAM, *J. Electrochem. Soc.* **132** (1985) 2854.
42. I. EPELBOIN, C. GABRIELLI, M. KEDDAM and H. TAKENOUTI, in "Comprehensive Treatise of Electrochemistry", Vol. 4, "Electrochemical Materials Science", edited by J. O' M. Bockris, B. E. Conway, E. Yeager and R. E. White (Plenum Press, New York, 1981) pp. 151–92.
43. M. A. HABIB and J. O' M. BOCKRIS, in "Comprehensive Treatise of Electrochemistry", Vol. 1, "The Double Layer", edited by J. O' M. Bockris, B. E. Conway, E. Yeager and R. E. White (Plenum Press, New York, 1980) pp. 135–219.
44. A. J. BARD and L. R. FAULKNER, "Electrochemical Methods. Fundamentals and Applications" (Wiley, New York, 1980).

Received 23 January
and accepted 20 November 1995